# We are IntechOpen, the world's leading publisher of Open Access books Built by scientists, for scientists

**6,900**
Open access books available

**186,000**
International authors and editors

**200M**
Downloads

**154**
Countries delivered to

Our authors are among the

**TOP 1%**
most cited scientists

**12.2%**
Contributors from top 500 universities

CLARIVATE ANALYTICS
**BOOK CITATION INDEX**
INDEXED

**WEB OF SCIENCE**™

Selection of our books indexed in the Book Citation Index
in Web of Science™ Core Collection (BKCI)

## Interested in publishing with us?
Contact book.department@intechopen.com

Numbers displayed above are based on latest data collected.
For more information visit www.intechopen.com

# Typical Internal Defects of Gas-Insulated Switchgear and Partial Discharge Characteristics

Fuping Zeng, Ju Tang, Xiaoxing Zhang, Siyuan Zhou and Cheng Pan

Additional information is available at the end of the chapter

## Abstract

Gas-insulated switchgear (GIS) is a common electrical equipment, which uses sulfur hexafluoride ($SF_6$) as insulating medium instead of traditional air. It has good reliability and flexibility. However, GIS may have internal defects and partial discharge (PD) is then induced. PD will cause great harm to GIS and power system. Therefore, it is of great importance to study the intrinsic characteristics and detection of PD for online monitoring. In this chapter, typical internal defects of GIS and the PD characteristics are discussed. Several detection methods are also presented in this chapter including electromagnetic method, chemical method, and optical method.

**Keywords:** GIS, internal defects, PD, intrinsic characteristics, electromagnetic detection method, chemical detection method, optical detection method

## 1. Introduction

Gas-insulated switchgear (GIS) is an electrical equipment that conceals traditional electrical devices in a chamber. GIS has obvious advantages over traditional air-insulated switchgear (AIS). Firstly, GIS demands less area thus reducing the cost; secondly, GIS has a longer overhaul period; and finally, GIS has higher reliability. For these reasons, GIS has been widely used in the world nowadays [1–4]. However, GIS has a complex structure that internal defects may come into being during process of manufacturing, transferring, and installing [5, 6]. These defects will induce partial discharge (PD) [7–9], which causes potential internal insulation aging. The insulation aging may develop into serious fault and blackout [10, 11]. PD also reflects GIS insulation state. By monitoring PD signals, potential defects can be recognized.

## 1.1. Typical types of GIS internal defects

There are several types of GIS internal defects, namely high-voltage (HV) conductor protrusions, free metal particles, floating potential, insulator metal pollution, and insulator gap [7]. The various defects in GIS are shown in **Figure 1**.

In recent decades, GIS has also been deployed widely in China. However, operating experience shows that although GIS equipment has high reliability, inevitable internal defects will still lead to failure and gradually major accidents. This has become a hot topic in power system [12].

According to statistics, the State Grid Corporation of China had a total of 48,498 GIS equipment in operation by the end of 2013, with a growth of 17.8% of the previous year. In the same year, 11 trips occurred in the GIS operation of the national grid system in China. CIGRE 23.10 Working Group GIS Fault Investigation Report shows that in all failures of GIS that occurred before 1985, the insulation failure accounted for 60 and 51% after 1985. According to operation analysis of the State Grid of China, at the end of June in 2008, 33 GIS accidents occurred including 24 insulation accidents, while operation failure occurred 74 times including 13 insulation accidents [4]. GIS insulation failure accidents are diverse. According to **Figure 2**, insulation faults caused by bad contact and defects of metal particles occupy a larger proportion [12].

In this chapter, we will focus on four typical types of GIS internal insulation defect, that is, free-metal particles, conductor protrusions, insulator gap, and insulator metal pollution.

### 1.1.1. Free metal particles defect (denoted as P-type defect)

Free-metal particles defects in GIS are one of the main causes of insulation failure. During the GIS assembling, installation or operation process, its metal parts may rub against each other, thus creating free metal particles. Due to their small size, these metal particles will move and beat under the electric field forces. If the range of particle movement is large enough, it is possible to form conductive paths or arc passages between the HV conductor and the shell, causing serious damage to the GIS. The path forming depends on many factors including applied voltage, shape and size of particles, and the position of the particles [12].
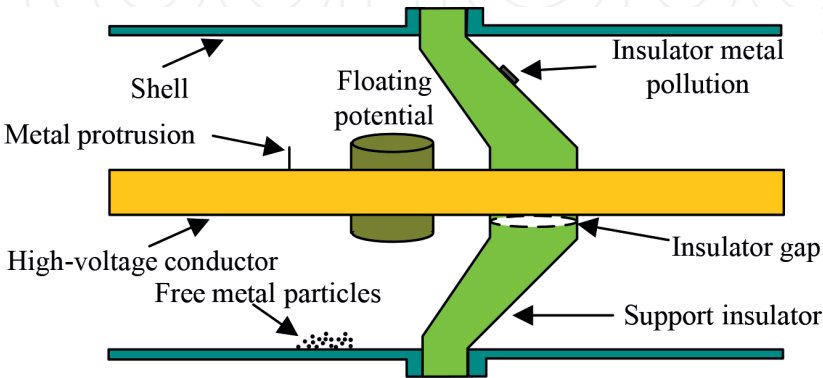


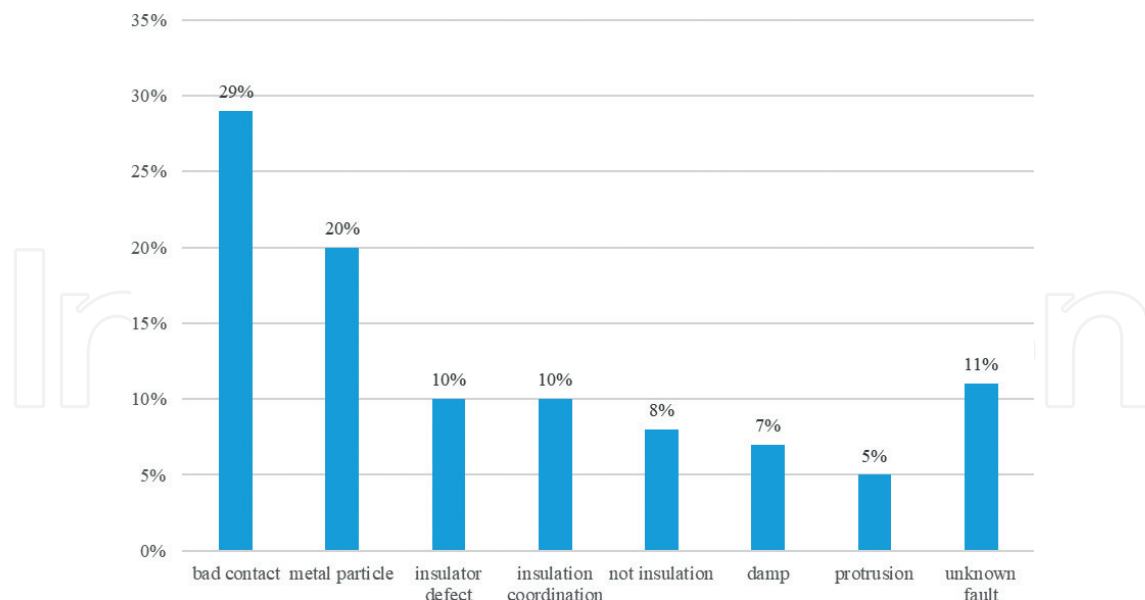**Figure 1.** GIS internal insulation-defect type diagram.

**Figure 2.** GIS equipment-defect type statistics.

### 1.1.2. Metal protrusions defect (denoted as N-type defect)

Metal protrusion defects refer to the defects that form on the protruding parts such as HV conductor inside GIS. Just like free-metal particles defect, these protrusions are usually formed during process of assembling, installation, or operation. Due to the sharp tip of the protrusions, the electric field will be distorted and strong electric field will then come into being. Under the rated working voltage, the strong electric field will induce a stable PD, but under some overvoltage, it may cause breakdown and GIS fault.

The discharge characteristics of protrusion on HV conductor and that on inner wall of shell are different. Protrusions on the HV conductor usually discharge in the negative half-cycle of the power frequency, while protrusions on the inner wall of the shell usually discharge in the positive half-cycle of the power frequency. Some tiny protrusions will be ablated in long-term discharge and will not threaten the insulation of GIS. However, larger protrusions will persist for a long-time and damage the operation insulation of GIS [12].

### 1.1.3. Insulator gap defect (denoted as G-type defect)

Insulator gap defects in GIS mainly happen on the basin-type insulator, which can be clas- sified into two types. One type is due to internal bubbles of epoxy resin resulting during process of manufacturing. Then during operation, PD will take place in these bubbles under strong electric field, resulting in gradual insulation deterioration of the basin-type insulator, and serious insulation breakdown may follow;

The other type is due to electric force in the long-term operation. Mechanical vibration process may result in connection loosening of basin-type insulator and HV conductive rod connection loosening. Then an insulator gap defect forms and induces PD, resulting in deterioration of the insulating properties of the basin-type insulator [13].

### 1.1.4. Insulator metal pollution defect (denoted as M-type defect)

The surface of the insulator sometimes adsorbs some metal particles which move under the electric field force. Some of the particles may not be dangerous at first, but due to the mechanical vibration under electrostatic force, their movement facilitates the discharge and then induces the PD.

Due to strong adsorption, some of the particles will not move. Particles fixed on the insulator surface forms insulator surface pollution defects. These fixed metal particles have the following characteristics: on their surface, charges will accumulate, and these surface charges sometimes aggravate the distortion of the electric field, causing PD. Particle-induced discharge will cause insulator surface damage, resulting in surface tree marks. Eventually, it may cause serious insulation breakdown and flashover [14].

## 1.2. Typical detection methods of PD

Under the operating voltage, the insulation defect will cause the local electric field distortion in the insulation medium. When the local electric field reaches the critical breakdown field strength, PD will be induced and a large amount of charged particles will be generated. Charged particles under electric field will migrate, recombine, and adhere, resulting in pulse current, and accompanied by optical, electrical, thermal, and acoustic effects. By effective detection of these signals, PD can be measured in the GIS. At present, there are five commonly used PD signal detection methods, that is, pulse current method [15], ultra-high frequency (UHF) method [16], ultrasonic method, chemical detection method, and optical detection method [17, 18]. In this chapter, we will focus on the following three PD signal detection methods:

### 1.2.1. UHF method

When a PD occurs, a non-periodically changing current pulse excites a changing magnetic field and radiates a high-frequency electromagnetic (EM) wave through the insulator. Due to the short-duration of the PD current pulse and the steep rising edge, the excitation frequency of the EM wave ranges from several MHz to several GHz [19, 20].

Because GIS is a good coaxial waveguide structure, high-frequency EM waves can be effectively transmitted within the GIS. Through the high-frequency sensors installed inside or outside GIS, the detection of these EM signals and PD signals can be achieved. This method is called UHF method.

The UHF method has many advantages. Firstly, it uses the UHF signal to avoid EM interference due to low frequency in the power grid and has strong anti-interference ability. Secondly, it can pinpoint the location of the PD [21]. Finally, this method has a large detection range and requires fewer sensors to be installed [11, 22].

### 1.2.2. Chemical detection method

Many studies show that the $SF_6$ gas will decompose under PD and the decomposed components will further react with moisture and oxygen in the gas chamber of GIS to generate a

series of chemical substances including $SO_2F_2$, $SOF_2$, $CF_4$, $SO_2$, $SOF_4$, $S_2F_{10}$, $SiF_4$, HF, CO, $CO_2$, $CH_4$, and $SF_4$. By detecting these decomposed components in the GIS gas chamber, it is possible to determine whether there is a PD source [23, 24].

Studies have shown that PD sources caused by different types of defects differ in $SF_6$ decomposition components, their ratio, and gas generating rate. So one can also identify the PD type by detecting $SF_6$ decomposition components.

$SF_6$ decomposition component method is able to locate the fault to find fault gas chamber, response accurately and timely to sudden failure, and judge the type of defect. It is also free from the scene of EM and noise interference, and regular detection can reflect the development of PD in GIS.

### 1.2.3. Optical detection method

In the process of PD, molecular ionization, ion recombination, and atomic energy level transition will excite and radiate optical signals. Optical detection methods of PD based on ultraviolet light (UV), infrared ray (IR), and visible light have been developed.

The spectral range of optical signal generated by PD in $SF_6$ gas is roughly 460–550 nm, which is mainly visible light. The basic principle of optical detection method is to use optical sensors to receive optical signals generated by the PD source and convert optical signals into electrical signals through the optical converter [17, 18].

Optical detection is not affected by strong EM interference on site, its anti-interference ability is more outstanding than the other two methods, and real-time monitoring of GIS PD phenomenon can be achieved. However, due to poor-optical signal transmission and GIS is a closed structure of equipment, the optical method cannot be used for outer GIS detection; optical sensors must be installed inside the GIS.

## 2. Physical model of typical defects and the electrical field simulation

In order to simulate GIS insulation defects and PD, what we choose for the physical model of insulation defect designed in this chapter is stainless steel, aluminum, and brass, and the solid insulation material is epoxy resin [25].

### 2.1. Typical detection methods of PD construction of insulation defect physical model

#### 2.1.1. N-type defect

Under steady-state AC voltage, the prominent parts are distributed in the electric field and form the local high field strength zone. This corona sometimes appears to be relatively stable as the discharge only occurs in a local area instead of throughout the entire electrode. In this chapter, pin-plate electrodes are used to simulate N-type defects. As shown in **Figure 3**, the pin electrodes are used to simulate abnormal protrusions on HV conductors and the plate electrodes simulate the metal shell of GIS.
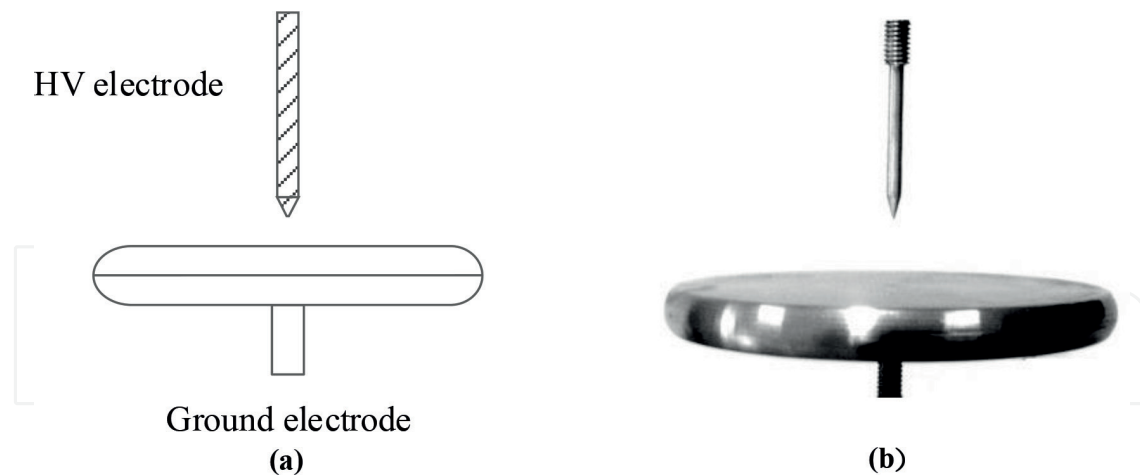
**Figure 3.** N-type insulation defect model. (a) Model diagram and (b) physical diagram.

In order to obtain a stable PD, an electrode is adopted with a tip radius of curvature of about 0.3 mm as well as a cone angle of 30°, and a ground plate electrode diameter of 120 mm as well as 10 mm thickness. Aluminum needle electrodes are designed and manufactured, with ground electrode material stainless steel, and electrode surface all were well polished.

### 2.1.2. P-type defect

Conductive particles have the shape of powder, flake or large solid particles, etc.; they get the charge in the electric field and will move or beat under electrostatic force. If the electric field is strong enough and the energy obtained by the conductive particles is large enough, particles are possible to cross the gap between the shell and the HV conductor or move to a point where the insulation is damaged.

The motion intensity of the conductive particles depends on the material, the shape, and the applied voltage, as well as the strength and duration of the external electric field strength and the location of the particles in GIS cavity. When the metal particles come close without touching the HV conductor, then PD arises as the electrical characteristics. Half of the actual GIS equipment uses a structure with a coaxial cylinder between the HV conductor and the shell, that is, a slightly uneven electric field structure [26]. In order to effectively simulate the slightly heterogeneous electric field structure of the coaxial cylinder inside the real GIS, the ball-bowl electrode shown in **Figure 4** is selected in this chapter. The bowl electrode is cut by a half of a stainless steel hollow sphere. In order to ensure the steady PD experiment, it is necessary to limit the beating range of the copper scrap. HV terminal ball electrode diameter is designed to be 44 mm, the ground bowl diameter is designed to be 120 mm, and particle maximum beating range up to 40 mm.

### 2.1.3. M-type defect

Due to electric force, some metal particles are absorbed on the insulator, thus distorting the insulator surface electric field and causing PD. Some metal particles on the insulator may not be dangerous at first, but under mechanical vibration and electric force, there will be slight movement and potential danger. Metal particles on the surface of the insulator will form surface charge aggregation, thereby increasing the possibility of failure. Particle discharge can cause
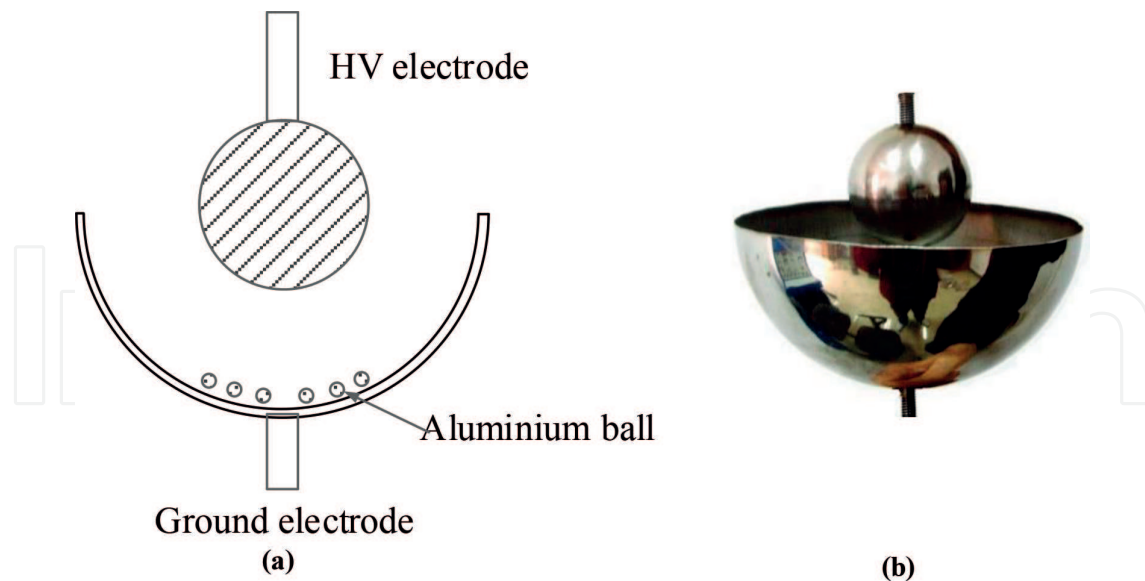
**Figure 4.** P-type insulation defect model. (a) Model diagram and (b) physical diagram.

damage to the surface of the insulator, causing surface tree marks in the power frequency field. Once the discharge channel is formed, a serious insulation accident will be caused.

In this chapter, rectangular copper cutting ($5 \times 18$ mm$^2$) is used to stimulate M-type defect. The contact surface of electrodes and cylindrical insulator is polished to avoid potential air gap discharge. The model structure is shown in **Figure 5**. The plate diameter is 120 mm, the epoxy resin cylindrical insulator diameter is 60 mm, and the thickness is 25 mm. The HV electrode material is aluminum, and the ground plate electrode material is stainless steel.

### 2.1.4. G-type defect

G-type defects are often formed in the manufacturing process such as epoxy curing shrinkage and internal voids [17]. The mechanism of air gap discharge is complicated, and it is generally believed that there are three ways of air gap discharge, that is, the throughout discharge, the discharge along the surface of the upper and lower electrode and the discharge along the air gap wall. In this chapter, G defects model is shown in **Figure 6**. The cylindrical insulator and the grounding electrode are closely adhered with epoxy glue to ensure that there are no gaps or bubbles between them. The air gap size at the interface between the high voltage plate electrode, and the insulator is about 1–3 mm. In order to reflect the real air gap situation, the insulator is slightly concave at the center of the upper surface, and the edge of the air gap is arc shaped.

### 2.2. Insulation defect electric field simulation

In this chapter, the finite-element analysis software COMSOL is used to simulate the electric field distribution of four insulation defect models. The simulation results are used to evaluate the feasibility of the model and provide the preliminary data reference for the following PD test.

In the simulation, a cylindrical cavity is used to simulate the SF$_6$ discharge gas chamber. The solution domain is set as SF$_6$ and the boundary conditions are grounded. The specific technical parameters of the simulation model and the relative dielectric constants are shown in **Tables 1** and **2**.
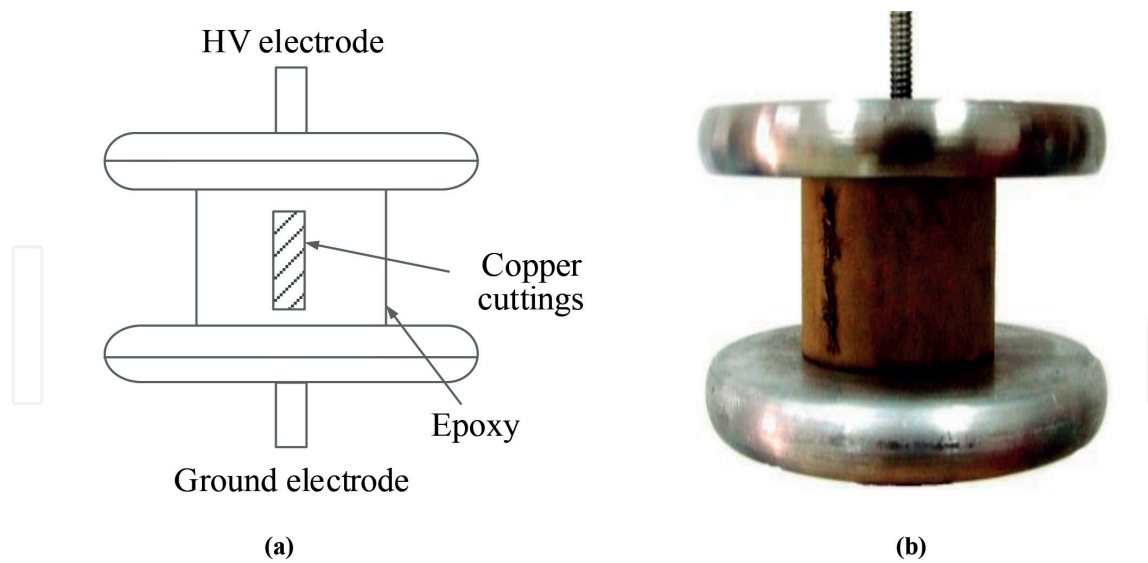
(a)                                                              (b)

**Figure 5.** M-type insulation defect model. (a) Model diagram and (b) physical diagram.



(a)                                                              (b)
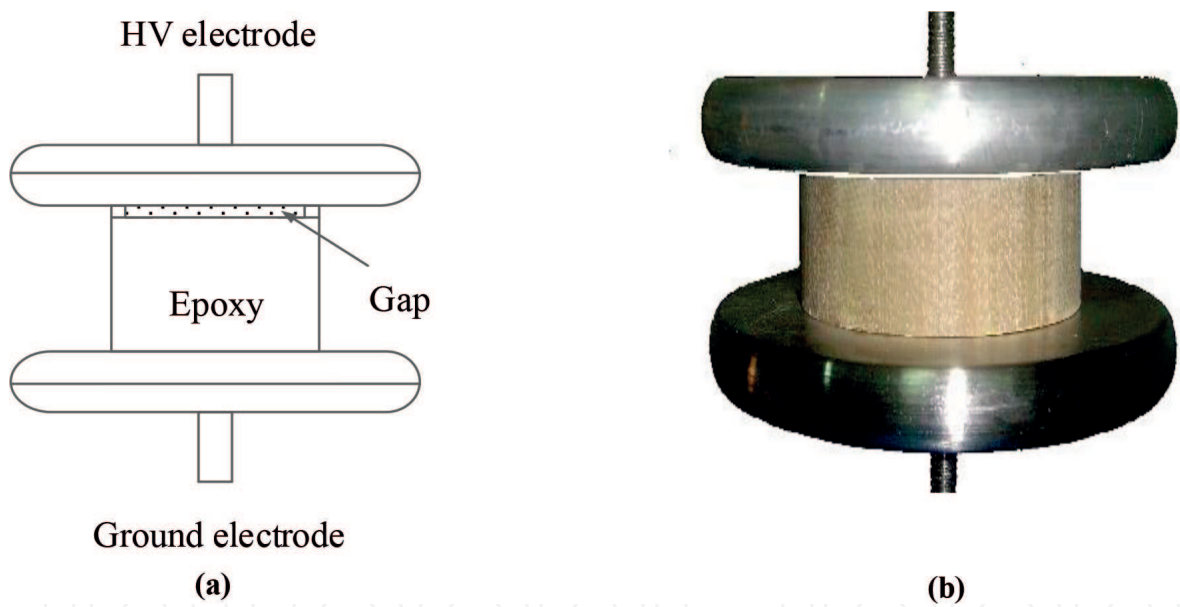
**Figure 6.** G-type insulation defect model. (a) Model diagram and (b) physical diagram.

### 2.2.1. N-type insulation defect

Due to the axial symmetry of N-type insulation defect, a two-dimensional axisymmetric model is adopted in this chapter. The HV-terminal needle electrode potential is set to 25 kV, the plate electrode with the cavity shell boundary is set to ground, and the needle-plate spacing is set to 10 mm.

The results of the electric field simulation of N-type insulation defect are shown in **Figure 7**. It can be seen from the figure that the distribution of the electric field between the needle and plate is extremely uneven. The electric field strength value at the tip of the needle electrode is high, and the electric field distortion at the tip of the needle electrode reaches up to 351 kV/cm.

| Cavity height/mm | Cavity diameter/mm | Plate electrode diameter/mm | Plate electrode thickness/mm | Needle curvature radius/mm | Cone sharp corners/° | Insulator diameter/mm | Insulator thick-ness/mm |
|---|---|---|---|---|---|---|---|
| 350 | 180 | 120 | 10 | 0.3 | 30 | 60 | 25/20 |

**Table 1.** Model technical parameters.

| Material | SF6 | Aluminum | Stainless steel | Aerosols (Copper) | Epoxy resin |
|---|---|---|---|---|---|
| Relative permittivity | 1.002 | 1.0 | 1.0 | 8000 | 3.8 |

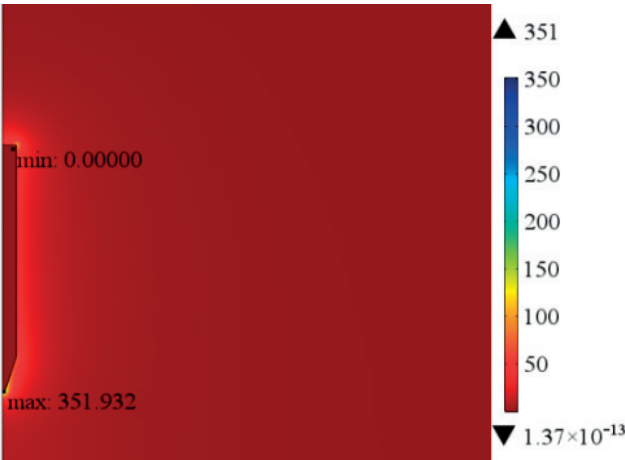**Table 2.** Relative dielectric constant of each part of the material.



**Figure 7.** N-type insulation defect space electric field simulation output (mm).
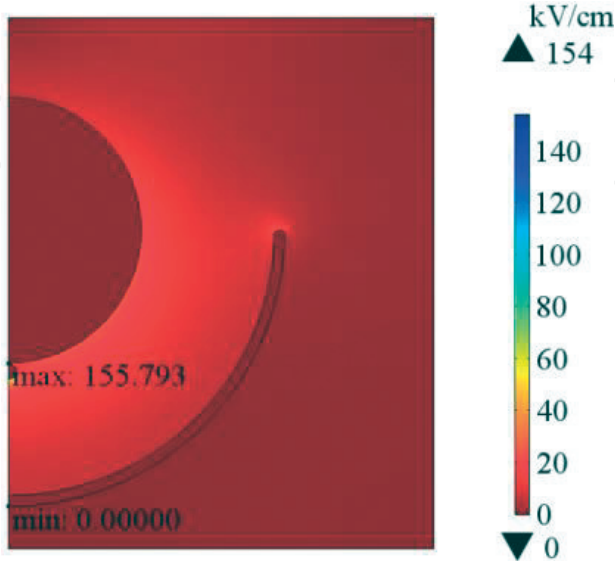


**Figure 8.** P-type insulation defect space electric field simulation output.

### 2.2.2. P-type insulation defects

Like N-type insulation defect, P-type insulation defect is also axisymmetric, so a two-dimensional axisymmetric model is adopted again for P-type insulation defect. In the simulation, the potential of the HV terminal ball electrode is set to be 30 kV, and the potential of the bowl electrode is set to be grounded. The distance between the ball and the bowl is set to 30 mm, and metal particles with a diameter of about 2 mm are placed in the bowl electrode. The floating particles are treated with the virtual large dielectric constant method.

The results of the electric field simulation of the P-type insulation defects are shown in **Figure 8**. The metal particles cause a distortion of the electric field between the electrodes. When the electric force is greater than the gravity of the metal particles, the particles will move or beat under the force. It can be seen from the figure that the electric field on the surface of metal particles close to the high voltage end is seriously distorted, and the maximum field strength reaches 155 kV/cm.

### 2.2.3. M-type insulation defects

In the simulation, the electrode potential of the HV terminal plate is set to be 30 kV, the boundary of the lower plate electrode and the cavity are set to be grounded, the thickness of the cylindrical insulator is set to 25 mm, and the surface is pasted with a metal copper cuttings of about $5 \times 18$ mm$^2$.

As shown in **Figure 9**, the simulation results show that the electric field at the surface of the insulator where the metal pollutants are located has been distorted, forming a very uneven field with the maximum field strength of 192 kV/cm. Based on the simulation results, insulator surface metal contamination will lead to PD before the insulator flashover.

### 2.2.4. G-type insulation defects

In the simulation, the potential of HV board is set to 60 kV. The boundary between lower board electrode and cavity is grounded. The upper surface of insulator is slightly concave with an average thickness of 20 mm. Between the HV board is arc-shaped air gap, with maximum gap 2 mm.
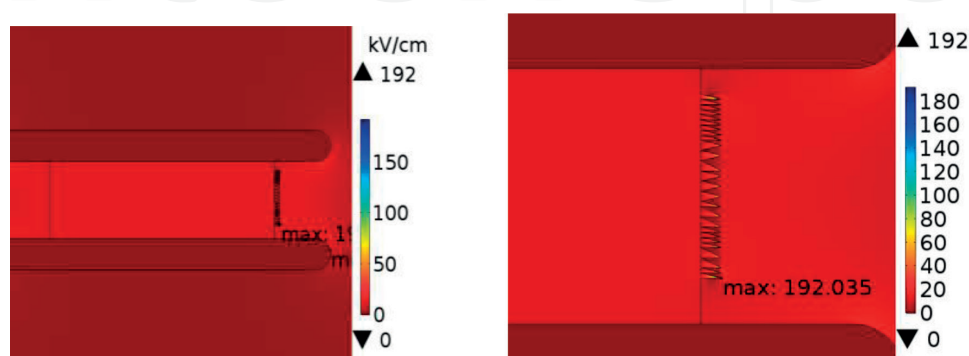


**Figure 9.** M-type insulation defect space electric field simulation output.
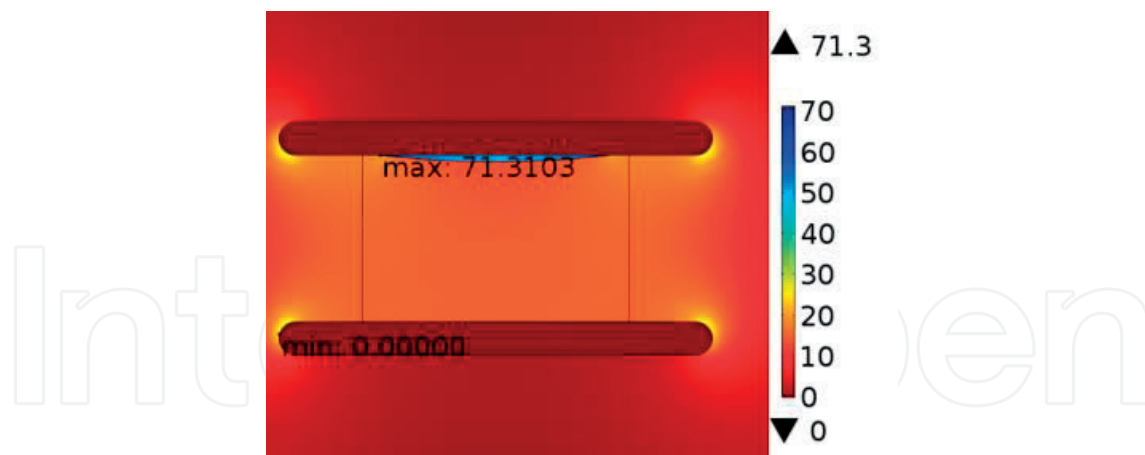
**Figure 10.** G-type insulation defect space electric field simulation output.

As shown in **Figure 10**, the simulation results of the electric field are mainly concentrated in the air gap between the high-voltage conductor and the insulator. The maximum field strength is 71.3 kV/cm. From the simulation results, G-type insulation defect has higher initial discharge voltage.

## 3. UHF characteristics of typical defects PD

As mentioned in Section 1, PD can be detected by UHF method. In this section, UHF characteristic of PD will be discussed. Experiments and analysis will be shown as follows.

### 3.1. Experimental setup

The detecting and measuring platform for PD is shown in **Figure 11**. The regulator (T1) input voltage is 220 V, the output voltage is adjustable from 0 to 250 V, the regulator output voltage through non-halo test transformer (T2: 10 kVA/50 kV) is boosted as the test voltage and is applied to the test object through a 10 kΩ protection resistor ($R_r$). The protection resistor is used to limit the amplitude of the short circuit current which may appear after the breakdown of the test object. To measure the test voltage, a capacitor divider in parallel on both ends of the test object is used [27]. The experimental voltage is acquired by outer UHF antenna developed by the authors (ultra-high frequency microstrip antenna, with 340–440 MHz bandwidth) and displayed on the digital storage oscilloscope (DSO: Lecroy WavePro 7100). The DSO has the largest sample rate of 20 GS/s.

### 3.2. Data acquiring and processing

Experiments can be done on the platform in **Figure 15**. Large numbers of data can then be acquired and processed. All sampling data are unified and normalized, so that the resulting mathematical models are more universal [28]. Unification means that each PD signal consists of 10,000 sampling points at a sampling rate of 20 GS/s (i.e., the sampling time is 500 ns, the sampling step is 0.05 ns, and the trigger point is set at the 4000th point). Normalization means that each value of the sample points is divided by the maximum absolute value.
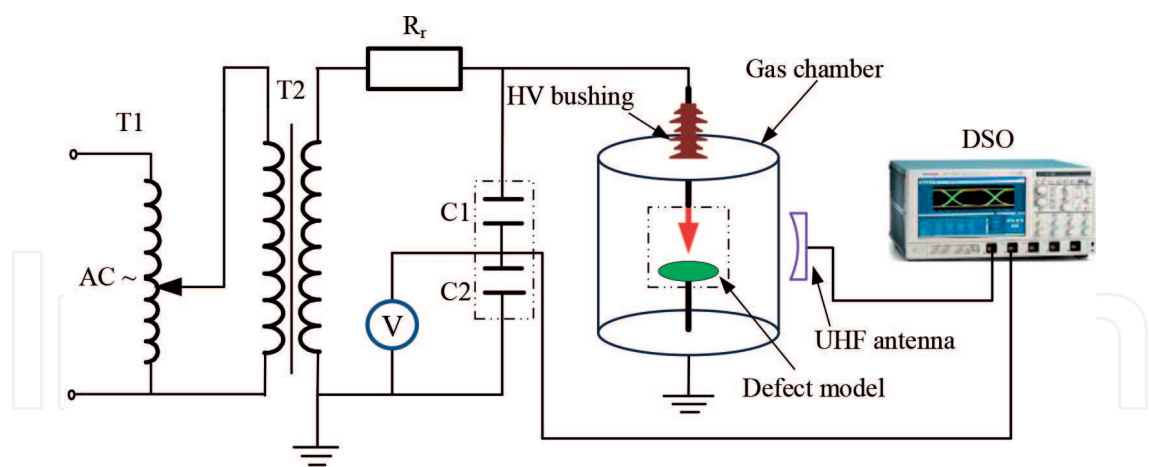
**Figure 11.** Detecting and measuring platform.

| Types of defects | Coefficients | Value | Coefficients | Value | Coefficients | Value |
|---|---|---|---|---|---|---|
| N-type | a1 | 0.2002 | b1 | 4852 | c1 | 435.3 |
| | a2 | 0.1863 | b2 | 4444 | c2 | 215.2 |
| | a3 | −0.9328 | b3 | 3998 | c3 | 19.2 |
| | a4 | 0.3613 | b4 | 6097 | c4 | 769.7 |
| | a5 | −0.3475 | b5 | 5767 | c5 | 119 |
| P-type | a1 | 0.2858 | b1 | 4305 | c1 | 39.6 |
| | a2 | 0.2332 | b2 | 4531 | c2 | 97.7 |
| | a3 | 0.1117 | b3 | 4762 | c3 | 104.1 |
| | a4 | −0.9565 | b4 | 3998 | c4 | 19.1 |
| | a5 | 0.0454 | b5 | 6181 | c5 | 211.8 |
| M-type | a1 | 0.9757 | b1 | 4000 | c1 | 23.2 |
| | a2 | 0.7679 | b2 | 5298 | c2 | 521.2 |
| | a3 | 0.7750 | b3 | 6661 | c3 | 606.1 |
| | a4 | 1.1040 | b4 | 5951 | c4 | 591.9 |
| | a5 | −1.5420 | b5 | 5981 | c5 | 1006.0 |
| G-type | a1 | 1.0100 | b1 | 3998 | c1 | 30.3 |
| | a2 | 0.0588 | b2 | 5156 | c2 | 358.2 |
| | a3 | 0.8981 | b3 | 4368 | c3 | 177.9 |
| | a4 | −1.0730 | b4 | 4358 | c4 | 201.4 |
| | a5 | 0.0232 | b5 | 7225 | c5 | 152.5 |

**Table 3.** Parameters of different types of defect.

Mathematical models of PD for VHF measurement are established by fitting to Gaussian plots function, the selected mathematical model is [28]:

$$f(x) = \sum_{i=1}^{n} a_i \bullet e^{-\frac{(x-b_i)^2}{c_i^2}} \tag{1}$$

where $a_i$, $b_i$, and $c_i$ are parameters and different of defects have different parameters. Based on massive experiment data, these parameters can be calculated as shown in **Table 3**.

**Figures 12–15** show time domain and frequency domain UHF PD characteristics, and they, respectively, denote G-type defect, M-type defect, N-type defect, and P-type defect. In time domain, the unit of x-axis is nanosecond, while in frequency domain, the unit of x-axis is gigahertz. Notice that the y-axis in time domain and frequency domain has no unit because it represents normalized data, that is, the U* and A* both stand for per unit.
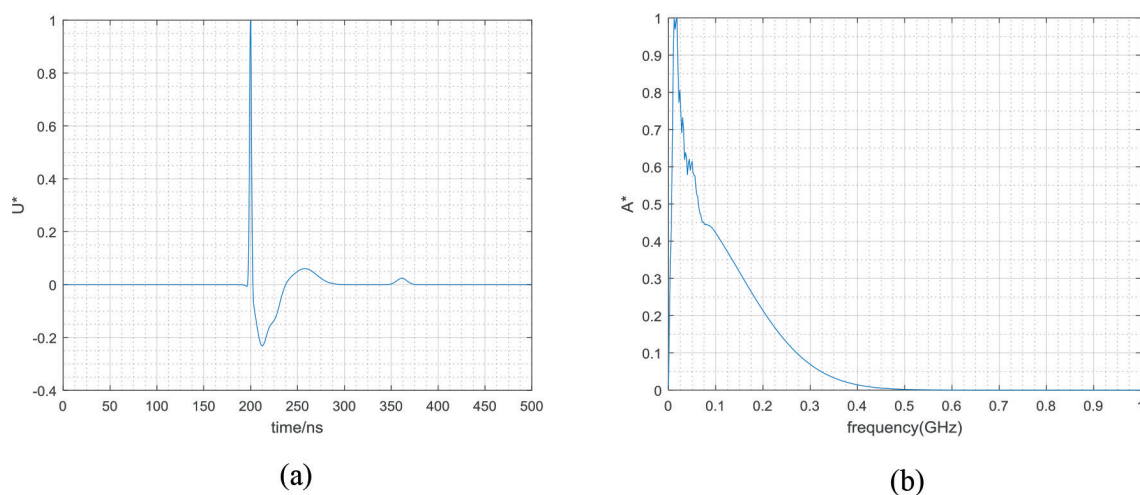


(a)                                                                           (b)

**Figure 12.** G-type defect UHF PD characteristics. (a) Time domain and (b) frequency domain.



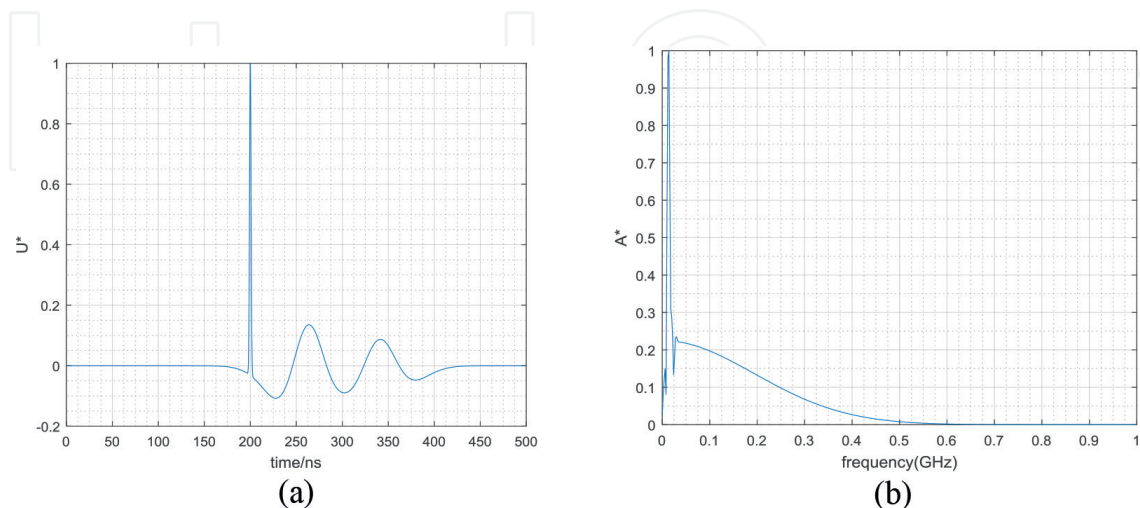(a)                                                                           (b)

**Figure 13.** M-type defect UHF PD characteristics. (a) Time domain and (b) frequency domain.
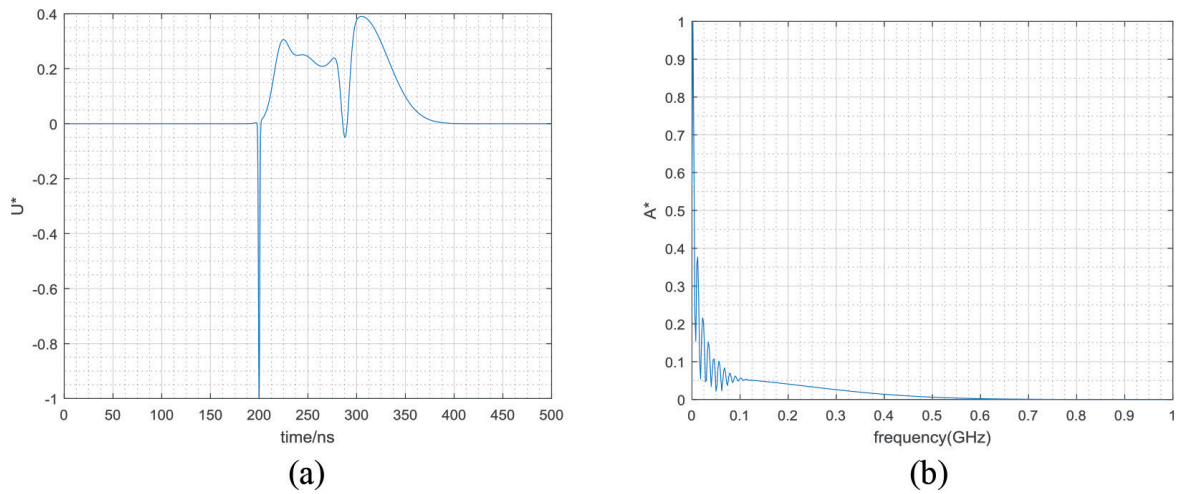
**Figure 14.** N-type defect UHF PD characteristics. (a) Time domain and (b) frequency domain.
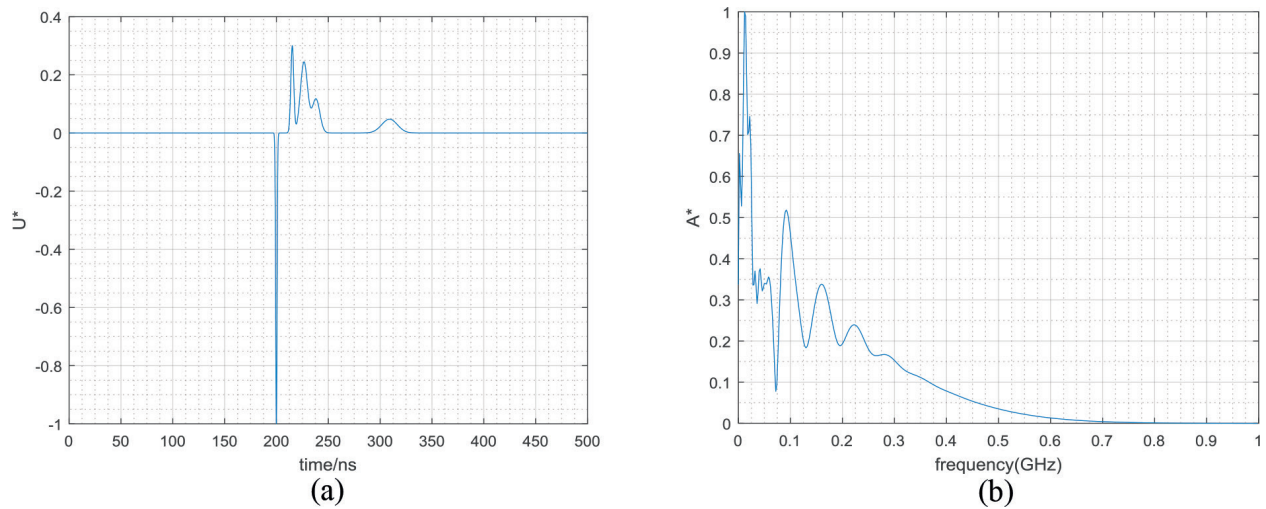


**Figure 15.** P-type defect UHF PD characteristics. (a) Time domain and (b) frequency domain.

For G-type defect characteristics curve, in time domain, there is a sharp jump at the 4000th point, and the curve is smooth after the jump; while in frequency domain, there is a jump after the original point, and the curve is smooth after the jump except for some protuberant points. For M-type defect characteristics curve, in time domain, there is a sharp jump at the 4000th point, and the curve is smooth after the jump with two peaks; while in frequency domain, there is a jump after the original point with a smaller jump afterwards, and the curve is smooth except for some protuberant points. For N-type defect characteristics curve, in time domain, there is a sharp jump at the 4000th point toward the negative direction, and the curve is smooth after the jump with a flat segment and then two peaks; while in frequency domain, there is oscillation on the whole frequency axis. For P-type defect characteristics curve, in time domain, there is a sharp jump at the 4000th point toward the negative direction, and several peaks follow afterwards; while in frequency domain, there is a jump after the original point with several oscillations afterwards.

## 4. Chemical characteristics of typical defects PD

In GIS, PD takes place accompanied by $SF_6$ decomposition. In addition, different defects will lead to different decomposition components. Based on this idea, chemical methods can be used to detect PD [23].

### 4.1. Experimental setup

The detecting and measuring platform for PD is shown in **Figure 16**. The measuring platform is similar to that in Section 3.1, but the UHF antenna will be replaced by gas chromatography mass spectrometry (GCMS), with its type Shimadzu QP-2010 Ultra.

The experiment is carried out in the gas chamber, which is closed filled of $SF_6$ gas with a specific pressure. Certain type of insulation defects for PD is also placed in the chamber. The coupling capacitor (Ck: 500 pF/100 kV) provides a high frequency and low-impedance path to the pulsed current and is converted to a voltage signal via a sense-less impedance ($Z_m$: 50 Ω), and it is displayed by digital storage oscilloscope. The decomposed components generated under PD are detected by GCMS.

### 4.2. Experimental steps

In this chapter, $SF_6$ decomposition experiments under four types of insulation defects are carried out. Under each type, the experiments last for 96 h. The decomposition gas is collected every 12 h, and the concentration of characteristic decomposition components $CF_4$, $CO_2$, $SO_2F_2$ is measured. The initial discharge voltage and the test voltage of various insulation defects are shown in **Table 4**. The experimental process is as follows:

1.  The insulation defect model is installed in $SF_6$ partial discharge decomposition gas chamber, the vacuum chamber is first evacuated and then filled with fresh SF6 gas, and then evacuated. Repeat the process until the chamber is filled with pure 0.2 MPa $SF_6$.

2.  Connect the test circuit according to **Figure 20**, and then adjust the regulator to slowly increase the test voltage until the oscilloscope can detect PD on the defect model. Record the experimental voltage $U_0$ at this time, that is, the initial discharge voltage. Then, continue to raise at the experimental voltage.

3.  Every 12 h, $SF_6$ gas is collected. The single collection gas volume is about 100 mL. Gas chromatograph is used to analyze the concentration of gas components.

4.  After a 96-h continuous experiment on a defect model, another model of the defect will replace it and continue the experiment according to the aforementioned steps until all four types of defects are all done.

### 4.3. $SF_6$ decomposition characteristics

The decomposition components under the four types of defects are shown in **Figure 17(a)–(d)**, that is, N-type, M-type, P-type, and G-type defect, respectively. Four characteristic
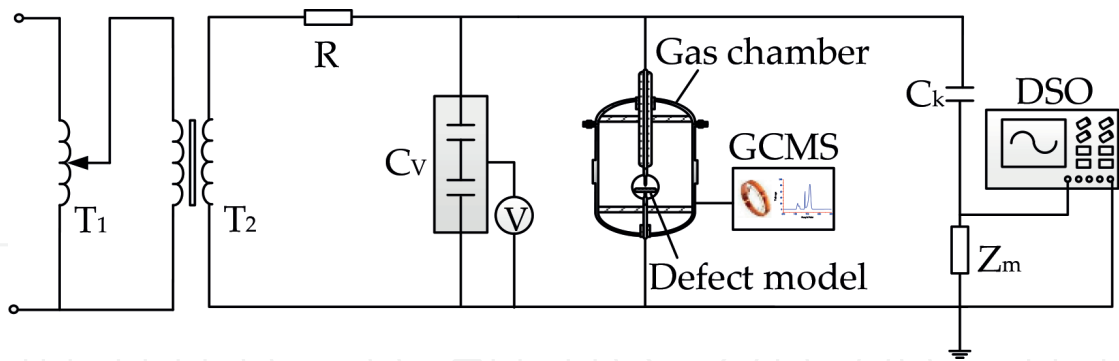
**Figure 16.** Detecting and measuring platform.

| Voltage | Defect type | | | |
|---|---|---|---|---|
| | N-type (kV) | M-type (kV) | P-type (kV) | G-type (kV) |
| Starting discharge voltage | 16.2 | 21.6 | 17.5 | 25.7 |
| Experimental voltage | 19.4 | 25.9 | 21.0 | 30.8 |

**Table 4.** Test voltage under different insulation defects.

decomposition components are generated, but the amounts of different characteristic components are quite different.

Under the N-type defect, at the end of the experiment, that is, at 96 h, concentration of $SOF_2$ was as high as 1114.5 μL/L, $SO_2F_2$ was 471.2 μL/L, $CO_2$ was 124.8 μL/L, and $CF_4$ was only a few μL/L. It was detected in the experiment that the concentration of components in ascending order is $SOF_2 > SO_2F_2 > CO_2 > CF_4$. Concentrations of $SOF_2$, $SO_2F_2$, and $CO_2$ all have an almost linear increase, indicating that PD is stable. The gas production rate dropped within a few tens of hours before the end of the experiment. It is preliminarily inferred that the moisture and oxygen in the gas chamber decreased after being consumed in experiment, resulting in a corresponding slowdown of various chemical reaction rates. Although the concentration of $CF_4$ generally increases, it does not increase simply linearly, and even decreases sometimes. The reason for this is that concentration of $CF_4$ is too low. Although the gas chromatograph detector sensitivity is very high, the final calculation of the test results needs to be integrated on the resulting chromatographic peak, when the concentration result is low, the impact of integral error will be greater.

The decomposition components under the M-type defect are shown in **Figure 17(b)**. The amounts of different characteristic components are also different. However, compared with the N-type defect, the difference is much smaller. At 96 h, concentration of $SOF_2$ was 42.78 μL/L, concentration of $SO_2F_2$ was 14.95 μL/L, concentration of $CO_2$ was 2.18 μL/L, and concentration of $CF_4$ was 6.18 μL/L. In the experiment, the concentration of components in ascending order is $SOF_2 > SO_2F_2 > CF_4 > CO_2$. Concentration of $SOF_2$ and $SO_2F_2$ gradually increased, but their increasing rate gradually decreased, especially $SO_2F_2$. Its concentration almost stopped increasing at the end of the experiment. That is because the insulator
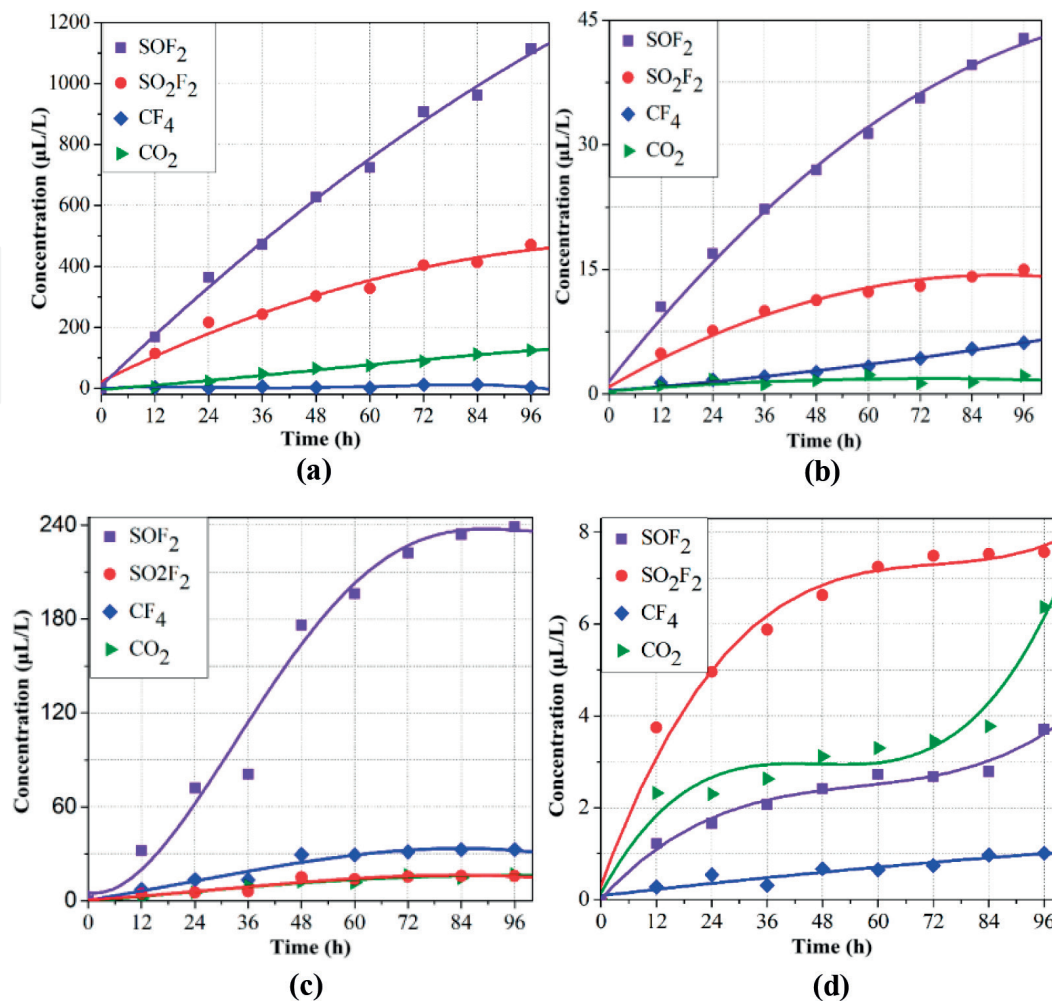
**Figure 17.** Decomposition concentration under four types of defects. (a) N-type defects, (b) M-type defects, (c) P-type defects, and (d) G-type defects.

surface contamination is gradually ablated by discharge; its effect on the electric field distortion becomes weaker and weaker, resulting in gradual decrease in discharge intensity. Because of sufficient fluorine atoms generated by the discharge and carbon atoms provided by the insulator, $CF_4$ is relatively less affected by the discharge intensity and its concentration increases substantially linearly with time. The increase of $CO_2$ does not simply grow linearly, and sometimes even decreases. The main reason for this is the concentration of $CO_2$ is low under M-type defect, and the integral error of the gas chromatograph has a greater impact on it.

The characteristic decomposition components under the P-type defect are shown in **Figure 17(c)**. Under this defect, four characteristic decomposition components were also generated. At 96 h, the concentration of $SOF_2$ was 238.9 μL/L, the concentration of $SO_2F_2$ was 15.82 μL/L, the concentration of $CO_2$ was 16.63 μL/L, and the concentration of $CF_4$ was 32.68 μL/L. The concentration of components in ascending order is $SOF_2 > CF_4 > CO_2 > SO_2F_2$. The concentration of the four characteristic components did not increase linearly. In the first 24 h of the experiment, the components concentration increased linearly, and the increasing rate was larger; from 24

to 36 h, the concentration of components also increased, whereas the increasing rate dropped sharply; from 36 to 48 h, the increasing rate rapidly increased. After 48 h, the increasing rate decreased slowly. At the end of the experiment, all characteristics components concentration almost stopped increasing. The main reason for this is that the discharge formed by the defects of P-type defect is unstable; the free particles are moved under strong electric field force due to their small mass. Only when moved to the position conducive to discharge will the particles lead to discharge. These particles may move randomly, which will lead to unstable discharge.

The characteristic decomposition components under G-type defect are shown in **Figure 17(d)**. The concentration of the four characteristic decomposition components under the insulation defect is low. At the end of the experiment, the concentration of $SOF_2$ was 3.71 µL/L, the concentration of $SO_2F_2$ was 7.57 µL/L, the concentration of $CO_2$ was 6.37 µL/L, and the concentration of $CF_4$ was 1.01 µL/L. The concentration of components in ascending order is $SO_2F_2 > CO_2 > SOF_2 > CF_4$. There is no obvious regularity in the increasing of concentration of the four characteristic components. The time-varying increasing rate is mainly due to the unstable PD, sometimes the discharge is very intense, and sometimes discharge stops. In addition, the overall discharge repetition rate is not high, resulting in the overall concentration of decomposition products not high and growth not regular.
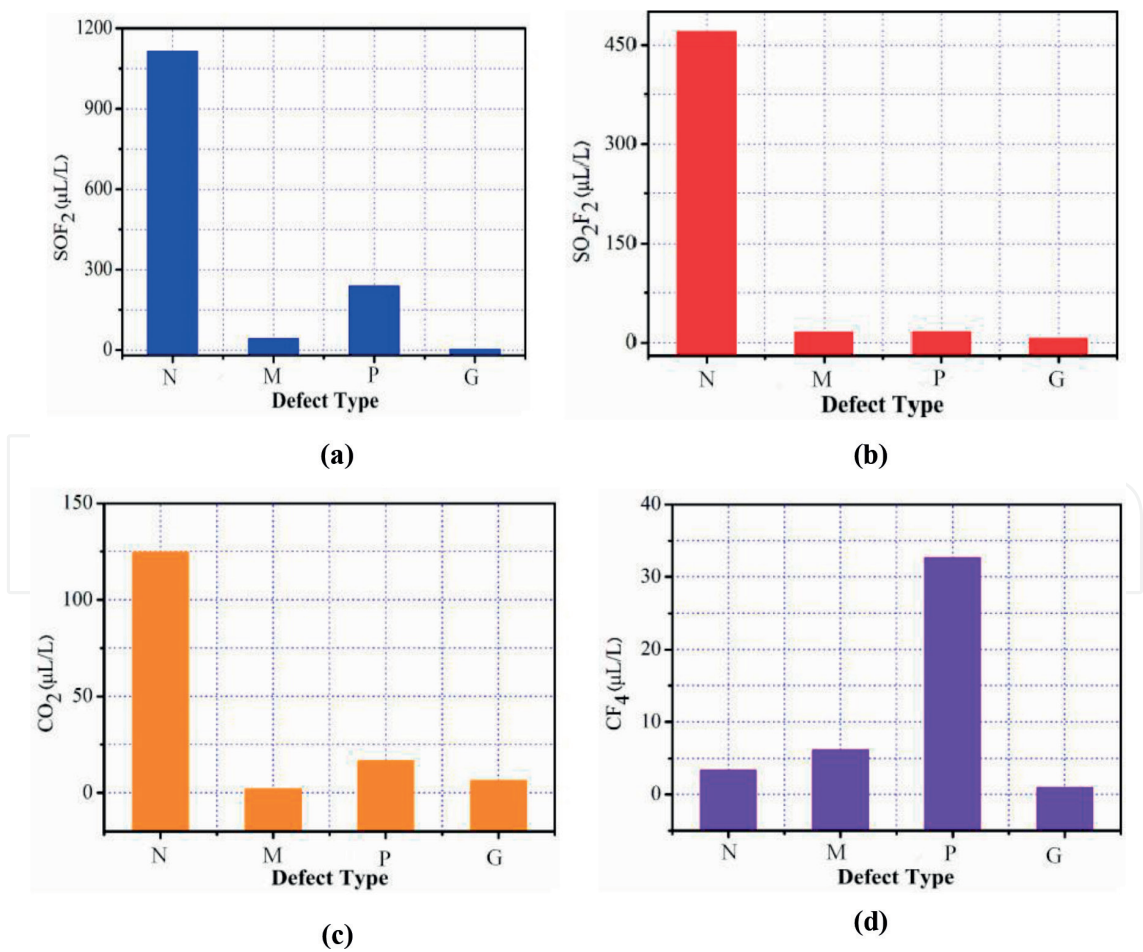


**Figure 18.** Decomposition components amount under four types of defects. (a) $SOF_2$ amount, (b) $SO_2F_2$ amount, (c) $CO_2$ amount, and (d) $CF_4$ amount.

A conclusion of $SF_6$ decomposition component under four types of insulation defects can be drawn that, amounts and ratio of decomposition components are different under different defects. Under each defect, the decomposition components under four types of defects compared with each other is as shown in **Figure 18**. For example, the amount of $SOF_2$ is higher than $SO_2F_2$ under the N-type defect, whereas the amount of $SO_2F_2$ in G-type defect is higher than $SOF_2$. The decomposition amounts of $CF_4$ and $CO_2$ also vary with different types of defects, more $CO_2$ is detected under N-type defect, and only a smaller amount of $CF_4$ is detected. Under P-type defect, the amount of $CF_4$ is larger than that of $CO_2$. Under M-type defect, only a small amount of $CO_2$ is detected; under G-type defect, both $CF_4$ and $CO_2$ are detected, but the concentration of $CO_2$ is higher than that of $CF_4$. Under N-type and M-type defects, the decomposition components increasing rate is stable, which is due to the reason that PD is stable under the two defects. In contrast, under P-type and G-type defects, PD is unstable. The reason is that particles and gap is not conducive to stable PD. The repetition rate varies with time, as well as the discharge amplitude. Especially under P-type defect, due to movement of metal particles, concentrations of decomposition components vary most intensively.

# 5. Optical characteristics of typical defects PD

In GIS, PD will ionize $SF_6$ molecules, and electrons will release and gain energy during the ionization process. When the electrons release energy, they will release photons at the same time, which are called luminescence; the positive and negative ions after ionization also recombine to release photons and become a composite light. Optical measurement uses photoelectric sensors to detect PD in the light intensity it generated to determine its strength. For optical measurement of signal generated by PD in GIS, detection system is less affected by outside interference and has higher sensitivity of measurement. It can detect PD in real time and identify the position of PD. Therefore, it can be used for on-line monitoring of PD in GIS.

At present, there are mainly two ways to detect the optical signal generated by PD in the GIS by optical measurement: one is to directly use the photoelectric sensor to detect the optical signal generated by the PD; the other is to insert the optical fiber sensor into the GIS to detect the optical signal generated by the PD. The former is more flexible to install, but the detection range is smaller, whereas the latter installation is more fixed, but the detection range is larger. Different types of insulation defects lead to different optical signals released by the PD, so the PD can be identified and diagnosed by using the optical measurement [12].

## 5.1. Experimental setup

The schematic diagram of the fluorescence optical fiber sensing system used to study the optical characteristics of the typical defects is shown in **Figure 19**. The optical fiber sensor system mainly comprises an optical sensor unit, optical transmission unit, photoelectric conversion unit, power supply module, and electrical signal transmission and acquisition unit [12].

Four types of single-defect models in this paper are respectively put into the device. After the preparation, the experimental device is applied with the experimental voltage. Slowly raise the test voltage and record the initial discharge voltage of the four single-defect models. Continue to
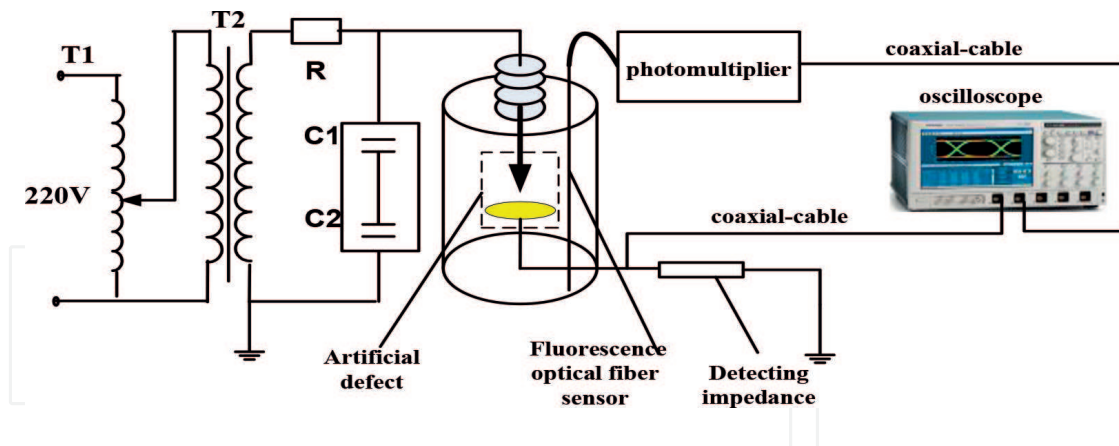
**Figure 19.** Figure of the fluorescent fiber sensor system.

slowly increase the experimental voltage and collect PD signal of different discharge intensity. Because PD signal of every power frequency cycle needs to be collected, a reference voltage signal should be introduced before the PD signal is collected to correct the phase of PD. Oscilloscope sampling frequency is set to 50 Ms/s, the total acquisition signal length 20 ms, and sampling points 1 M. In experiments, the fluorescent fiber sensing system stores signals in a time domain waveform. Therefore, PD light pulses must be extracted from the time-domain waveform that record the PD signal for each cycle. The method comprises the following steps: set a threshold firstly according to noise amplitude and extract a PD light pulse whose amplitude is greater than the threshold and record and store the amplitude and corresponding phase of the PD light pulse.

### 5.2. $\phi$-$u$-$n$ distribution characteristics of photodetector PDs with different defects

In this chapter, the $\varphi$-$u$-$n$ spectral is used to analyze PD. In $\varphi$-$u$-$n$ space, $\varphi$ represents the phase of PD power frequency, $u$ represents the amplitude of PD light pulse signal, character-izing the PD discharge level, and $n$ represents the number of discharges. The space surface is constructed by dividing the power-frequency phase $\varphi$-axis into 256 intervals from 0° to 360° and dividing the amplitude of the optical pulse signal from 0 to 0.1 V into 128 small sections so that the $\varphi$-$u$ plane is divided into 128 × 256 cells; count $\varphi$-$u$ plane discharge times within each cell, and one can get the space surface. The $\varphi$-$u$-$n$ space surface constructed in this paper is based on 200 power-frequency signals. The three-dimensional map of the different defects obtained from the collected PD data is shown in **Figure 20**. There is a significant difference between the three-dimensional spectra of the $\varphi$-$u$-$n$ obtained by detecting different internal defects in the GIS using the optical method.

For N-type defect, the repetition rate of light pulse is high, the average amplitude is large, the range of amplitude variation is small, and the light pulse distribution has obvious phase charac-teristics and symmetrical about 270° in phase. The reason is that the PD under N-type defect is a typical corona discharge which is relatively stable, the intensity of the single discharge is small, the light signal generated by the discharge is relatively stable, and the light intensity generated by the single discharge is relatively large. Therefore, the average amplitude of the detected light pulse is large, and the range of the amplitude is small. The initial discharge voltage of positive half cycle of corona discharge is higher than the negative half cycle of power frequency, and the
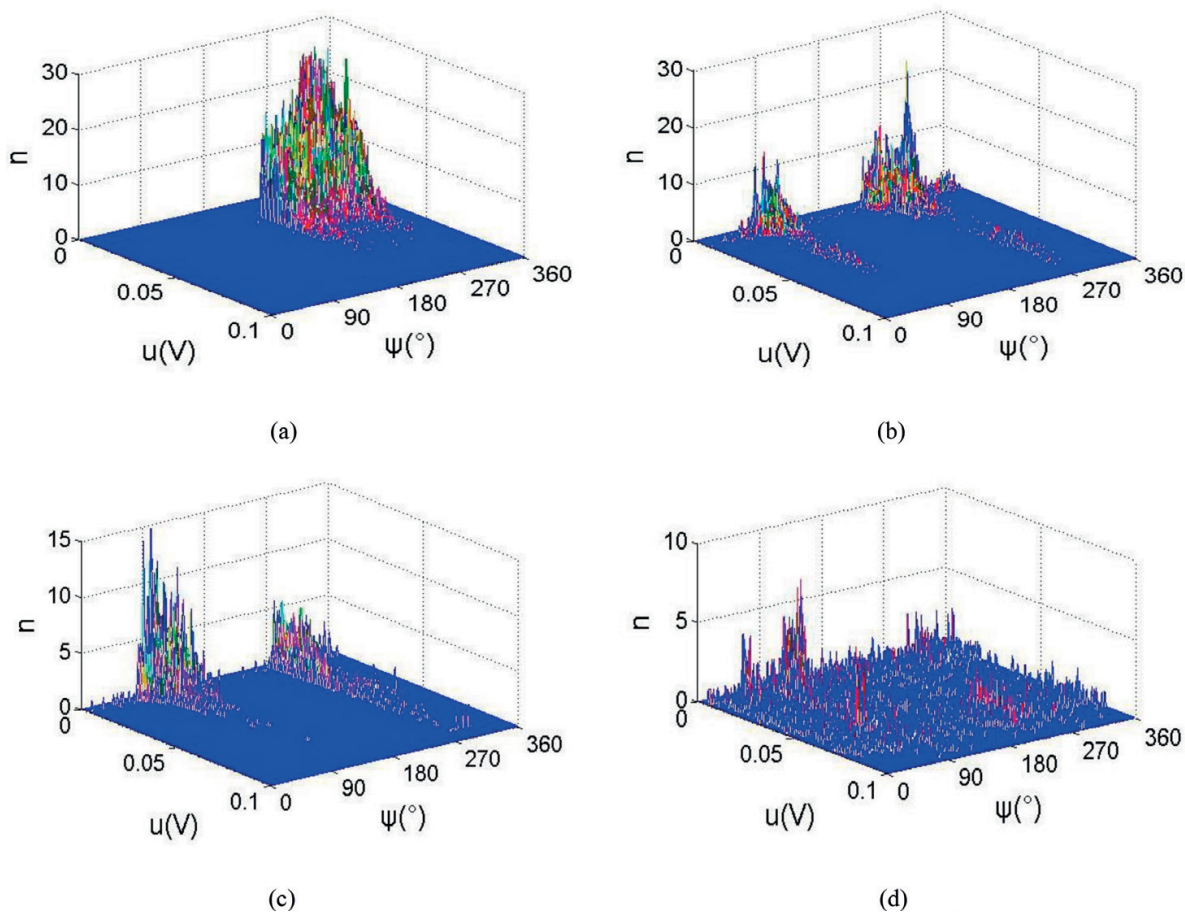
**Figure 20.** The *φ-u-n* chart of PD induced by the four types of defects in GIS. (a) N-type, (b) G-type, (c) M-type, and (d) P-type.

space charge generated by discharge diffuses rapidly in the gas. The influence of space charge on the external electric field is very small. The initial discharge voltage of corona discharge is almost equal to the extinction voltage. Therefore, the light pulses are distributed around the 270° phase of the negative half cycle of the power frequency and symmetrical about 270°.

For G-type defect, the pulse repetition rate is high, the average amplitude is small, the amplitude range is wide, and the light pulse distribution has obvious phase characteristics, which are all distributed at the phases of 90 and 270°. Phase width distributed in the 90–180° is greater than 0–90°, and 180–270° phase width greater than 270–360°. The reason is that the PD caused by the G-type defect between the insulator and the metal conductor is not very stable. The light intensity generated by a single discharge is not uniform, but the light intensity generated by the discharge is relatively small. Therefore, the average light pulse detected has small amplitude and large amplitude range. As the insulator hinders the spread of the space charge, the space charge will cause the distortion of the external electric field so that the initial discharge voltage caused by the air gap defect between the insulator and the metal conductor is higher than the extinction voltage. Therefore, the light pulse phase width distributed between 90 and 180° is greater than 0–90° and between 180–270° phase width is greater than 270–360°.

For M-type defect, the pulse repetition rate is low, the average pulse amplitude is small, the amplitude range is large, and the light pulse distribution has obvious phase characteristics

and is distributed around the phase 90 and 270°. Phase width distributed in the 90–180° is greater than 0–90° and in the 270–360° phase width is greater than 180–270°. The reason is that the PD produced by M-type defect will generate electrical branches on the surface of the insulator, which will affect the insulation of the insulator surface. As a result, the PD is not very stable, and the light intensity produced by a single discharge is different. However, the overall light intensity is relatively small, so the optical measurement method detecting average amplitude of the light pulse is small, with a wide range of amplitude.

For P-type defect, the pulse repetition rate is low, the average amplitude is large, the range of the amplitude changes is large, and the phase distribution of the light pulse is not characterized. The reason is that metal particles in the external electric field obtain the induced charge and will move under electric force. The movement intensity of the metal particles depends on the induced charges, the shape of the particles, the direction of movement of the particles, and whether the particles collide with other objects during the movement. PD generated by P-type defects is caused by the movement of the metal particles. Therefore, it is very unstable, and the phase of PD is also irregular.

# 6. Conclusion

In this chapter, typical defects in GIS are discussed and physical model is established, then different resulting PD is studied. Four typical defects and their respective PD UHF characteristics, chemical characteristics, and optical characteristics are then obtained by experiments. Different figures and data owing to different types of PD are compared with each other so that unique features could be further extracted.

As for UHF characteristics, it can be seen visually that waveforms of different defects have obvious difference. Then some parameters can be designed to measure the essential difference, which can be presented as fingerprints. In time domain, statistics parameters are selected as features. For example, these parameters include mean, variance, skewness, kurtosis, etc. While in frequency domain, these parameters also works. In addition, Shannon entropy, wavelet sub-band energy, and absolute value of peaks can also be included. Based on these features, methods such as support vector machine can be applied to classify the defects.

For chemical characteristics, it can be concluded that the $SF_6$ PD decomposition components amount under the four types of insulation defects are obviously different, and so is their ratio. So the insulation defect can be identified by detecting PD decomposition component of $SF_6$. Methods such as artificial neural network can then be set up to classify the defects. The concentration and ratio of each decomposition components are the input variables and during training process the defect is finally classified.

For optical characteristics, just as UHF characteristics, the spectrals of different defects have obvious difference. So some statistics parameters are introduced. Because the optical spectral has three dimensions, projection on two-dimension plane is firstly needed, and then parameters are extracted. The classification step is like that of UHF or chemical characteristics.

## Author details

Fuping Zeng*, Ju Tang, Xiaoxing Zhang, Siyuan Zhou and Cheng Pan

*Address all correspondence to: fuping.zeng@whu.edu.cn

School of Electrical Engineering, Wuhan University, Wuhan, China

## References

[1] Gu FC, Chang HC, Kuo CC. Gas-insulated switchgear PD signal analysis based on Hilbert-Huang transform with fractal parameters enhancement. IEEE Transactions on Dielectrics & Electrical Insulation. 2013;**20**(4):1049-1055

[2] Dai D et al. Feature extraction of GIS partial discharge signal based on S-transform and singular value decomposition. Iet Science Measurement & Technology. 2017;**11**(2):186-193

[3] Okabe S, Ueta G, Hama H, et al. New aspects of UHF PD diagnostics on gas-insulated systems. IEEE Transactions on Dielectrics and Electrical Insulation. 2014;**21**(5):2245-2258

[4] Cigre WG. 33/23-12 Insulation coordination of GIS: Return of experience, on site tests and diagnostic techniques. Electra. 1998;**176**(2):67-95

[5] Pearson JS, Hampton BE, Sellars AG. A continuous UHF monitor for gas-insulated substations. IEEE Transactions on Electrical Insulation. 1991;**26**(3):469-478

[6] Cavallini A, Montanari GC, Contin A, Pulletti F. A new approach to the diagnosis of solid insulation systems based on PD signal inference. IEEE Electrical Insulation Magazine. 2003;**19**(2):23-30

[7] Tang J, Zhou R, Wang DB, et al. Application of SA-SVM incremental algorithm in GIS PD pattern recognition. Journal of Electrical Engineering and Technology. 2016;**11**(1):192-199

[8] Koo JY et al. Identification of insulation defects in gas-insulated switchgear by chaotic analysis of partial discharge. Iet Science Measurement & Technology. 2010;**4**(3):115-124

[9] Gao W, Ding D, Liu W. Research on the typical partial discharge using the UHF detection method for GIS. IEEE Transactions on Power Delivery. 2011;**26**(4):2621-2629

[10] DEA M et al. Charge accumulation effects on time transition of partial discharge activity at GIS spacer defects. IEEE Transactions on Dielectrics & Electrical Insulation. 2010;**17**(1):247-255

[11] Zhang X et al. GIS partial discharge pattern recognition based on the chaos theory. IEEE Transactions on Dielectrics & Electrical Insulation. 2014;**21**(2):783-790

[12] Zhuo R. Feature optimization and fault diagnosis of GIS based on combined detection [PhD thesis]. Chongqing University; 2014 (in Chinese)

[13] Liu F. Decomposition characteristic of $SF_6$ under PD & recognition of PD category and calibration of impact factors [PhD thesis]. Chongqing University; 2013 (in Chinese)

[14] Wang Y. Decomposition characteristic of $SF_6$ under PD & recognition of PD category and calibration of impact factors [PhD thesis]. Chongqing University; 2013 (in Chinese)

[15] International Standard IEC 60270. High Voltage Test Techniques—Partial Discharge Measurements, 3rd ed. Geneva, Switzerland: International Electrotechnical Commission; 2000

[16] IEC-62478. High-Voltage Test Techniques—Measurement of Partial Discharges by Electromagnetic and Acoustic Methods. Proposed Horizontal Standard. 1st ed. Geneva, Switzerland: International Electrotechnical Commission (IEC); 2016

[17] Tao J. Study on partial discharge identification and harmfulness assessment for gas insulated switchgear [PhD thesis]. Chongqing University; 2013 (in Chinese)

[18] Ren M, Zhou J, Song B, Zhang C, Dong M, Albarracín R. Towards optical partial discharge detection with micro silicon photomultipliers. Sensors. 2017;**17**:2595

[19] Robles G, Albarracín R, Vázquez JL. Antennas in partial discharge sensing system. In: Chen ZN, editor. Handbook of Antenna Technologies. Singapore: Springer; 2015. pp. 1-47

[20] Álvarez Gómez F, Albarracín-Sánchez R, Garnacho Vecino F, Granizo Arrabé R. Diagnosis of insulation condition of MV switchgears by application of different partial discharge measuring methods and sensors. Sensors. 2018;**18**:720

[21] Fresno JM, Robles G, Martínez-Tarifa JM, Stewart BG. Survey on the performance of source localization algorithms. Sensors. 2017;**17**:2666

[22] Judd MD, Farish O, Hampton BF. The excitation of UHF signals by partial discharges in GIS. IEEE Transactions on Dielectrics and Electrical Insulation. 1996;**3**:213-228

[23] Tang J, Yang X, Ye G, Yao Q, Miao Y, Zeng F. Decomposition characteristics of $SF_6$ and partial discharge recognition under negative DC conditions. Energies. 2017;**10**:556

[24] Dong M, Zhang C, Ren M, Albarracín R, Ye R. Electrochemical and infrared absorption spectroscopy detection of $SF_6$ decomposition products. Sensors. 2017;**17**:2627

[25] Tang J et al. Partial discharge recognition through an analysis of $SF_6$ decomposition products part 2: Feature extraction and decision tree-based pattern recognition. IEEE Transactions on Dielectrics & Electrical Insulation. 2012;**19**(1):37-44

[26] Zhuo R et al. Study on relationship between optical signals and charge quantity of partial discharge under four typical insulation defects. Electrical Insulation and Dielectric Phenomena IEEE. 2013:1209-1212

[27] Dong Y. Research on feature extraction and severity assessment of partial discharge in GIS [master thesis]. Chongqing University; 2013 (in Chinese)

[28] Tang J et al. Study on mathematical model for VHF partial discharge of typical insulated defects in GIS. IEEE Transactions on Dielectrics & Electrical Insulation. 2007;**14**(1):30-38